



Effect of Additives on Shape Evolution during Electrodeposition

II. Parameter Estimation from Roughness Evolution Experiments

Effendi Rusli,^a Feng Xue,^a Timothy O. Drews,^a Philippe M. Vereecken,^{b,*}
Panos Andricacos,^{b,d} Hariklia Deligianni,^{b,*} Richard D. Braatz,^{a,*} and
Richard C. Alkire^{a,**,z}

^aDepartment of Chemical and Biomolecular Engineering, University of Illinois at Urbana-Champaign,
Urbana, Illinois 61801, USA

^bIBM Research Division, Thomas J. Watson Research Center, Yorktown Heights, New York 10598, USA

Numerical analysis procedures are used to identify the most sensitive parameters and estimate their values based on experimental measurements and a hypothesized mechanism for the effect of additives on copper electrodeposition. The electrolysis system consists of an acid copper sulfate bath containing accelerator, suppressor, and leveler additives in the range of concentrations typically used for deposition of on-chip wiring interconnections. Experimental measurements, obtained with an impinging jet apparatus, included surface roughness evolution and potential-time curves under constant current deposition in a set of 36 electrolyte compositions, selected by a D-optimal design procedure. The hypothesized additive mechanism consisted of a set of 15 surface reactions and 3 homogeneous chemical reactions. A mathematical model was composed that couples kinetic Monte Carlo simulation (for roughness evolution) with a finite volume method (for computing surface concentrations and potential). After identifying the most sensitive parameters and estimating their values, the surface concentrations of key species associated with the additive mechanism were simulated. The methods reported here are reusable and may be applied to other applications beyond the copper electrodeposition used here for its initial development.

© 2007 The Electrochemical Society. [DOI: 10.1149/1.2772425] All rights reserved.

Manuscript submitted February 5, 2007; revised manuscript received June 25, 2007. Available electronically September 4, 2007.

The mechanisms by which complex additive systems influence shape evolution during electrodeposition are generally uncertain due in large part to the difficulty in making direct experimental observations at the molecular scale. Because indirect observations, such as the deposit shape evolution itself, contain the integrated signature of the various molecular as well as macroscopic-scale phenomena, the measurement of surface roughness evolution data allow, in principle, the extraction of information about additive behavior. Engineering models, however, must produce accurate predictions with known error bars if they are to be suitable for design, optimization, and control. Therefore, the process of extraction of information about additive behavior requires a multiscale model and, in addition, a sufficiently large data set so that the most sensitive parameter values can be estimated accurately.^{1,2} In this work, experimental surface-roughness-evolution and other electrochemical data were obtained and analyzed numerically to estimate values of the most sensitive parameters in a multiscale model.

The technological application selected for demonstrating the method reported in this work is the electrodeposition of on-chip copper interconnects. Shape evolution during infill of small recesses depends critically on additive behavior³ in order to achieve bottom-up deposition (superconformal fill)⁴ and to avoid formation of voids. Although the exact compositions of commercial additives mixtures are held proprietary, systems for the electrodeposition of copper to form interconnects incorporate an accelerator, suppressor, and leveling agent which work synergistically to influence the deposit morphology.⁵⁻⁷ An important engineering challenge is to formulate the right additive combination that meets fabrication objectives as the technology matures (i.e., as wiring dimensions shrink). Various mechanisms for the concerted action by which additives influence shape evolution have been reported in the context of mathematical models based on the concept of competition for surface sites between accelerator and suppressor compounds⁴ combined with elements of transport, kinetics,⁷ and geometry.^{8,9} While con-

tinuum models are appropriate for predicting macroscopic behavior, they are less able to address surface roughness evolution at the microscopic scale.

Monte Carlo methods have been applied to a number of surface roughening/smoothing processes provided that a fairly complete mechanism for the surface reaction mechanism is known.^{10,11} We have recently demonstrated the linkage of a Monte Carlo simulation code with a macroscopic continuum code to compose a multiscale model for an electrodeposition application.¹² That approach was used in Part I of this series to compose a multiscale model for numerical simulation of roughness evolution in the presence of additives.¹³

A premise of this work is that roughness evolution data contain integrated information on the phenomena that control deposition. The quantitative deconvolution of such data therefore provides, in principle, information on how additives influence deposit growth. The reaction kinetic parameters associated with feature superfill chemistry are extracted from experimental observations of current density and roughness evolution on flat samples under well-characterized mass-transfer conditions. A mechanistic hypothesis for the role of additives was embedded in a multiscale model for predicting roughness evolution. Parameter sensitivity simulations were performed to identify the key parameters, which must be known accurately to produce a predictive model.^{14,15} An iterative model identification procedure¹⁶ was used to estimate the most sensitive parameters. In a subsequent publication, the parameters obtained in this work are used in simulations that are compared with additional experimental data on trench-infill for a range of solution compositions and deposition rates.^{17,18}

Experimental

Measurement of surface roughness evolution during electrodeposition was carried out on flat electrodes in order to facilitate high experimental throughput as well as low computational effort. Additional experimental details are available in a thesis.¹⁹ Figure 1 shows a cross section of the impinging jet electrochemical cell containing a reference electrode (RE, saturated mercurous sulfate) in the flow inlet and a counter electrode (copper wire) in the flow outlet. The working electrode (WE) was a featureless wafer (150 nm Cu on 15 nm Ta on SiO₂/Si) exposed to electrolyte flowing through two concentric glass tubes; the edge of the outside tube (1.8 mm i.d.) was coated with silicone sealant to prevent leakage, and the inner

* Electrochemical Society Active Member.

** Electrochemical Society Fellow.

^c Present address: IMEC v.z.w., 3001 Leuven, Belgium.

^d Deceased.

^z E-mail: r-alkire@uiuc.edu

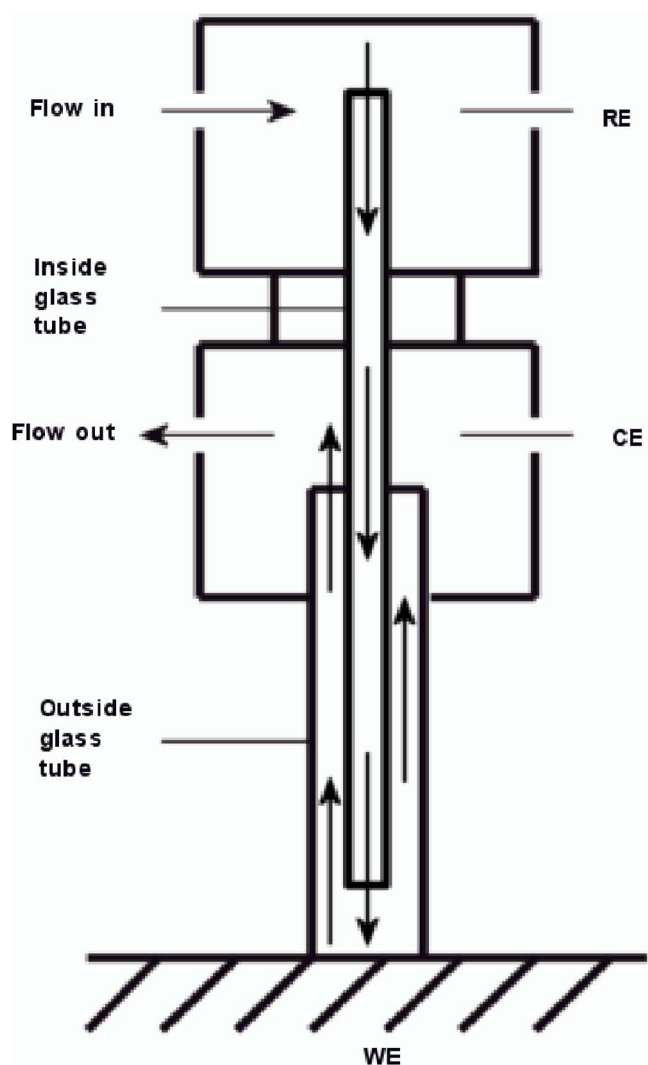


Figure 1. Schematic of impinging jet cell designed for high-throughput electrodeposition experiments that require biased immersion and rapid postelectrolysis rinsing of the specimen.

tube (0.6 mm i.d., 0.8 mm o.d.) was positioned 1 mm above the WE. A glass pump (Harvard, PHD 2000 Programmable) with silicone tubing and polypropylene fittings completed the flow system.

Solutions were prepared from CuSO_4 (Aldrich, 99.995%), H_2SO_4 (Aldrich, 99.999%), bis(3-sulfopropyl)disulfide (SPS, Mw 354, Rohm and Haas Electronic Materials L.L.C.), chloride (as HCl, Alfa Aesar, 99.999%), polyethylene glycol (PEG, Mw 3400, Aldrich), 1-(2-hydroxyethyl)-2-imidazolidinethione (HIT, Mw 146, Rohm and Haas Electronic Materials L.L.C.), and high-purity water (18 M Ω cm, Barnstead "E-pure" System). A D-optimal design procedure was used to select experimental conditions based on the choice of seven independent variables: (i) current density, and the concentrations of (ii) H_2SO_4 , (iii) CuSO_4 , (iv) Cl^- , (v) PEG, (vi) SPS, and (vii) HIT. The D-optimal design involved 36 sets of experiments, which are listed in Table I.

The average mass-transfer coefficient for the impinging jet electrochemical cell, obtained from auxiliary limiting current experiments (ferri/ferrocyanide on Au), compared favorably with simulations carried out with commercial software (Comsol). A flow rate of 0.6 m/s in the inner tube, chosen for the experiments here, corresponded to an average diffusion layer thickness of 5 μm . For the range of experimental conditions investigated, the simulations indicated that the local deposition rate was everywhere less than 15% of

the local limiting current density and, in addition, that the Wagner number was between 1.4 and 240, for which the potential distribution is uniform. The high mass-transfer condition was purposefully chosen so that the kinetic rate constants estimated by this procedure are not dependent on mass-transfer conditions. A change in mass-transfer conditions would alter the surface concentrations and thus, the reaction rates, but not the reaction rate constants. The impinging jet cell simulation was also used to estimate the ohmic resistance between WE and RE for each experimental condition listed in Table I, as shown in the next-to-last column.

Experiments were carried out under "hot immersion" conditions by which a constant current was applied (EG&G PAR 273A) immediately upon contact of a dry WE by electrolyte. For each of the operating conditions, a stop-and-repeat procedure was used in which each condition was performed for multiple durations (2, 5, 25, 50, 75, 100, 150, 200, 300, and 500 s), each of which were repeated three times. After the desired period of deposition, the cell was disassembled in less than 1 s, and the WE was rinsed with distilled water followed by air drying. The surface of each deposit was scanned by atomic force microscopy (AFM, Digital Instruments NanoScope E, 125 μm scanning head, Si_3N_4 tip mounted on 200 μm triangular cantilevers, force constant 0.12 N/m, scan rate 3.05 Hz). Each WE specimen was imaged ($5 \times 5 \mu\text{m}$, 512×512 data points) at eight different azimuthal locations at a position 0.6 mm from the center of the WE, where the local current density was close to the average value. A total of $36 \times 10 \times 3 \times 8 = 8640$ AFM images were obtained. The root-mean-square (rms) surface roughness was calculated with software developed in our lab, as described in Appendix A.²⁰

Additive Mechanism

Based on the chemical and electrochemical reactions for this system published recently,⁴ the hypothesized reaction mechanism summarized in Table II was selected for investigation. The mechanism includes 15 surface reactions (written as actions taken in a KMC code) and 3 homogeneous reactions (implemented in a finite volume code). The mechanism includes 12 species in the solution phase and 5 species that are confined to the surface. In Part I, the same reaction mechanism was used to test numerical procedures and to make initial estimates of the model parameters (reported in Table I in Part I).¹³ Also listed in Table I of Part I are relevant physical property data where known. The following text provides evidence in support of the hypothesized additive mechanism. Additional discussion of mechanistic details is available in a thesis.¹⁹

Reactions 1-3 in Table II describe the two-step copper reduction mechanism on bare copper sites with soluble intermediate Cu_{aq}^+ ions, where Reaction 1 is the rate-limiting step.²¹ Reaction 4 denotes the surface diffusion of Cu atoms. In the KMC code, only Cu atoms were allowed to move by surface diffusion, and their movement was restricted to only those surface sites that were not occupied by other adsorbates. Reactions 5-9 describe the "suppressor" mechanism. The adsorption reaction to form CuCl_{ads} ²²⁻²⁴ (Reaction 5) occurs only on unoccupied surface sites; adsorbed CuCl_{ads} may subsequently either dissociate to Cu_{aq}^+ and Cl_{aq}^- ions (Reaction 6), or be reduced to Cu atoms and Cl_{aq}^- ions (Reaction 7), or combine with a PEG_{aq} molecule to form the suppressor $\text{CuClPEG}_{\text{ads}}$ (Reaction 8). The suppressor physically blocks all the surface reactions on its site, except for the dissociation (and thus desorption) of $\text{CuClPEG}_{\text{ads}}$ itself (Reaction 9).²⁵⁻²⁷ Based on the reported size of adsorbed PEG,²⁵ one $\text{CuClPEG}_{\text{ads}}$ molecule covers ~ 40 bare copper sites.^{25,26} The adsorbed $\text{CuClPEG}_{\text{ads}}$ was considered to physically block mass transport of $\text{Cu}_{\text{aq}}^{2+}$ and Cu_{aq}^+ ions to active sites on the electrode surface, instead of forming solvated polymer electrolyte.²⁸ By this approach, the potential dependence of PEG_{aq} coverage occurs as a consequence of the potential dependence of CuCl_{ads} coverage.^{24,27,29}

The "accelerator" mechanism is described by Reactions 10-13 along with 16. Reaction 10 permits reduction of SPS_{aq} to thiolate $^-_{\text{aq}}$ ions which, due to the high pK of the RS-H bond, are expected to be

Table I. Experimental conditions determined by D-optimal design for seven input variables: the concentrations of Cu₂SO₄, H₂SO₄, SPS, PEG, Cl⁻, and HIT, and the current density *i*.

No.	CuSO ₄ (mol/L)	H ₂ SO ₄ (g/L)	SPS (ppm)	PEG (g/L)	Cl ⁻ (ppm)	<i>i</i> (A/cm ²)	HIT (ppb)	IR drop (mV)	σ (1/ Ω cm)
1	0.7	175	3.0	0.3	100	0.020	5	0.003	0.493
2	0.3	5	50.0	0.1	100	0.020	5	0.071	0.021
3	0.8	175	3.0	0.1	10	0.003	200	0.001	0.478
4	0.8	5	50.0	3.0	100	0.003	200	0.006	0.036
5	0.3	175	26.5	3.0	55	0.0115	5	0.002	0.543
6	0.7	5	3.0	0.1	100	0.003	200	0.006	0.036
7	0.3	5	3.0	3.0	10	0.020	5	0.071	0.021
8	0.3	5	50.0	0.3	10	0.003	5	0.011	0.021
9	0.8	175	50.0	0.1	10	0.020	5	0.003	0.478
10	0.8	5	3.0	3.0	10	0.003	200	0.006	0.036
11	0.8	175	3.0	3.0	10	0.003	5	0.001	0.478
12	0.3	5	3.0	3.0	100	0.003	5	0.011	0.021
13	0.8	175	50.0	3.0	10	0.003	200	0.001	0.478
14	0.8	5	50.0	0.1	55	0.003	50	0.006	0.036
15	0.8	5	3.0	0.1	10	0.0115	5	0.023	0.036
16	0.8	175	50.0	3.0	100	0.020	5	0.003	0.478
17	0.3	175	3.0	0.1	100	0.020	200	0.003	0.543
18	0.8	175	3.0	3.0	10	0.020	200	0.003	0.478
19	0.7	175	26.5	0.1	10	0.0115	50	0.002	0.493
20	0.3	175	50.0	0.3	10	0.020	200	0.003	0.543
21	0.8	5	26.5	0.3	55	0.020	5	0.041	0.036
22	0.7	45	50.0	3.0	55	0.003	5	0.002	0.171
23	0.3	5	3.0	0.1	10	0.020	200	0.071	0.021
24	0.3	45	3.0	0.1	55	0.003	5	0.001	0.186
25	0.8	5	3.0	3.0	100	0.020	200	0.041	0.036
26	0.3	45	26.5	3.0	100	0.020	200	0.008	0.186
27	0.3	175	3.0	3.0	10	0.003	200	0.001	0.543
28	0.3	45	50.0	0.1	10	0.003	200	0.001	0.186
29	0.3	5	50.0	3.0	55	0.0115	200	0.040	0.021
30	0.8	175	3.0	3.0	100	0.003	200	0.001	0.478
31	0.8	45	3.0	0.1	100	0.020	50	0.009	0.164
32	0.8	5	50.0	3.0	10	0.020	200	0.041	0.036
33	0.8	45	50.0	0.3	100	0.0115	5	0.005	0.164
34	0.8	175	50.0	0.1	100	0.020	200	0.003	0.478
35	0.8	175	26.5	0.1	100	0.003	5	0.001	0.478
36	0.3	175	50.0	0.3	100	0.003	50	0.003	0.493

unstable in the aqueous phase and thus acquire hydrogen ions to form MPS_{aq} via Reaction 16. Although there is no direct evidence that SPS can be reduced to MPS_{aq} on a copper electrode in acidic aqueous solution, it is known that organic disulfide compounds can be reduced step by step in organic solvents with high polarity.³⁰ Some authors considered the Cu(I)thiolate_{ads} to be generated from the reaction between cupric ions and MPS_{aq},³¹ while others suggest it is from the reaction between Cu⁺_{aq} ions and SPS_{aq}.^{4,32,33} Reaction 11 provides for the generation of Cu(I)thiolate_{ads} which is known to form a robust Cu-S bond.³⁴ In the KMC code, Reaction 11 is permitted to occur only on bare copper surface sites. The catalytic action of Cu(I)thiolate_{ads} on Cu reduction is realized via Reaction 13, for which it was assumed that Cu⁺_{aq} ions can be reduced adjacent to or, if no bare copper substrate site is available, "underneath" a site occupied by Cu(I)thiolate_{ads}. Adsorbed Cu(I)thiolate_{ads} can dissociate to Cu⁺_{aq} and MPS_{aq} via Reaction 12.

Reactions 14 and 15 describe the leveler mechanism involving HIT_{aq}. Although its detailed chemistry remains unclear, it may be possible that HIT_{aq} undergoes hydrolysis or electrochemical reduction under cathodic conditions, without convincing evidence we assume here that HIT_{aq} (or a derivate) is a strong ligand which displaces adsorbed Cu(I)thiolate_{ads}. That is, HIT_{aq} acts as an accelerator remover which poisons Cu(I)thiolate_{ads} via Reaction 14, and then releases itself via Reaction 15. The released HIT_{aq} continues to poison other surface sites occupied by Cu(I)thiolate_{ads}.

Mathematical Models and Methods of Analysis

The mathematical model was implemented by combining a kinetic Monte Carlo code (for simulation of roughness evolution) with a continuum code (for simulation of transport and reaction in the solution adjacent to the deposition surface). Numerical analysis of the models was carried out to identify the most sensitive parameters and to estimate their values by comparison of simulated results with experimental data (rms roughness and potential as a function of time). By an iterative sequence beginning with the set of initial estimates of parameter values, reported in Part I of this series,¹³ the most sensitive parameters were identified and their values were estimated.

Kinetic Monte Carlo and continuum models.— The kinetic Monte Carlo approach used for analysis of roughness evolution data considered electrodeposition onto a flat, featureless substrate, which corresponds to the experimental conditions. The general features of the code used in the present work were described previously,^{11,13} although the code used here was written from scratch with the objective to achieve significantly improved performance and numerical efficiency. A (2 + 1)D solid-on-solid³⁵ method implementing the Bortz-Kalos-Lebowitz³⁶ algorithm was used to simulate the surface reactions that take place on the copper surface during electrodeposition. Table II provides the KMC rate expressions used for each surface reaction in the hypothesized mechanism. The KMC code

Table II. Continuum and KMC rate formula for chemical reactions in the mechanism (Th = thiolate).

No.	Surface reactions	KMC rate (s ⁻¹)	Continuum rate (mol/m ² s)
1	$\text{Cu}_{\text{aq}}^{2+} + \text{e}^- \rightarrow \text{Cu}_{\text{aq}}^+$	$k_1[\text{Cu}^{2+}]\exp[-\alpha_1 F\eta/(RT)]$	$k_1[\text{Cu}^{2+}]\theta \exp[-\alpha_1 F\eta/(RT)]$
2	$\text{Cu}_{\text{aq}}^+ + \text{e}^- \rightarrow \text{Cu}_{\text{s}}$	$k_2[\text{Cu}^+]\exp[-\alpha_2 F\eta/(RT)]$	$k_2[\text{Cu}^+]\theta \exp[-\alpha_2 F\eta/(RT)]$
3	$\text{Cu}_{\text{s}} \rightarrow \text{Cu}_{\text{aq}}^+ + \text{e}^-$	$k_3 \exp[(1 - \alpha_2)F\eta/(RT)]$	$k_3 \exp[(1 - \alpha_2)F\eta/(RT)]$
4	$\text{Cu}_{\text{s}} \rightarrow \text{Cu}_{\text{s}}$	Lateral: $D \exp[-E_a/(RT)]/(2\Delta L^2)$ Diagonal: $D \exp[-E_a/(RT)]/(4\Delta L^2)$	—
5	$\text{Cu}_{\text{aq}}^+ + \text{Cl}_{\text{aq}}^- \rightarrow \text{CuCl}_{\text{ads}}$	$k_5[\text{Cu}^+][\text{Cl}^-]$	$k_5[\text{Cu}^+][\text{Cl}^-]\theta$
6	$\text{CuCl}_{\text{ads}} \rightarrow \text{Cu}_{\text{aq}}^+ + \text{Cl}_{\text{aq}}^-$	k_6	$k_6[\text{CuCl}]$
7	$\text{CuCl}_{\text{ads}} + \text{e}^- \rightarrow \text{Cu}_{\text{s}} + \text{Cl}_{\text{aq}}^-$	$k_7 \exp[-\alpha_7 F\eta/(RT)]$	$k_7[\text{CuCl}]\exp[-\alpha_7 F\eta/(RT)]$
8	$\text{CuCl}_{\text{ads}} + \text{PEG}_{\text{aq}} \rightarrow \text{CuClPEG}_{\text{ads}}$	$k_8[\text{PEG}]$	$k_8[\text{CuCl}][\text{PEG}]$
9	$\text{CuClPEG}_{\text{ads}} \rightarrow \text{CuCl}_{\text{ads}} + \text{PEG}_{\text{aq}}$	k_9	$k_9[\text{CuClPEG}]$
10	$\text{SPS}_{\text{aq}} + 2\text{e}^- \rightarrow 2\text{Th}_{\text{aq}}^-$	$k_{10}[\text{SPS}]\exp[-2\alpha_{10}F\eta/(RT)]$	$k_{10}[\text{SPS}]\theta \exp[-2\alpha_{10}F\eta/(RT)]$
11	$\text{Cu}_{\text{aq}}^+ + \text{MPS}_{\text{aq}} \rightarrow \text{Cu(I)Th}_{\text{ads}} + \text{H}_{\text{aq}}^+$	$k_{11}[\text{Cu}^+][\text{MPS}]$	$k_{11}[\text{Cu}^+][\text{MPS}]\theta$
12	$\text{Cu(I)Th}_{\text{ads}} + \text{H}_{\text{aq}}^+ \rightarrow \text{Cu}_{\text{aq}}^+ + \text{MPS}_{\text{aq}}$	$k_{12}[\text{H}^+]$	$k_{12}[\text{Cu(I)Th}][\text{H}^+]$
13	$\text{Cu}_{\text{aq}}^+ + \text{Cu(I)Th}_{\text{ads}} + \text{e}^- \rightarrow \text{Cu(I)Th}_{\text{ads}} + \text{Cu}_{\text{s}}$	$k_{13}[\text{Cu}^+]\exp[-\alpha_{13}F\eta/(RT)]$	$k_{13}[\text{Cu}^+][\text{Cu(I)Th}]\exp[-\alpha_{13}F\eta/(RT)]$
14	$\text{Cu(I)Th}_{\text{ads}} + \text{HIT}_{\text{aq}} \rightarrow \text{Cu(I)HIT}_{\text{ads}} + \text{MPS}_{\text{aq}}$	$k_{14}[\text{HIT}]$	$k_{14}[\text{HIT}][\text{Cu(I)th}]$
15	$\text{Cu(I)HIT}_{\text{ads}} + \text{H}_{\text{aq}}^+ + \text{e}^- \rightarrow \text{HIT}_{\text{aq}} + \text{Cu}_{\text{s}}$	$k_{15}[\text{H}^+]\exp[-\alpha_{15}F\eta/(RT)]$	$K_{15}[\text{Cu(I)HIT}][\text{H}^+]\exp[-\alpha_{15}F\eta/(RT)]$
Homogeneous chemical reactions in bulk electrolyte.			
16	$\text{MPS}_{\text{aq}} \leftrightarrow \text{H}_{\text{aq}}^+ + \text{Th}_{\text{aq}}^-$		$k_{16}[\text{MPS}]$ $k_{16}[\text{H}^+][\text{Th}^-]$
17	$\text{H}_2\text{SO}_{4\text{aq}} \rightarrow \text{HSO}_{4\text{aq}}^- + \text{H}_{\text{aq}}^+$		$k_{17}[\text{H}_2\text{SO}_4]$
18	$\text{SO}_{4\text{aq}}^{2-} + \text{H}_{\text{aq}}^+ \leftrightarrow \text{HSO}_{4\text{aq}}^-$		$k_{18}[\text{SO}_4^{2-}][\text{H}^+]$ $k_{18}[\text{HSO}_4^-]$

was coarse-grained, with a domain of 128×128 lattice points to span a $5 \times 5 \mu\text{m}$ surface; that is, each mesoparticle was 39.06 nm on each side. Mesoparticles were chosen to be one molecule high in order to be able to simulate the blocking effect of monolayer surface coverage of an adsorbed species. The number of molecules in a mesoparticle was computed based on the species packing density (see Table III). Additional details are available in a thesis.³⁷ Given the species concentrations and potential at the solid-liquid surface, the KMC code calculates the surface roughness evolution and the flux of each species.

The concentrations and potential needed by the KMC code were computed from a continuum code that was virtually identical to that reported previously in Part I,¹³ but revised to account for the geometry used here.³⁷ The finite-volume method was used to solve transient one-dimensional (1D) partial differential equations (PDEs) based on solution equations (electroneutrality and the reaction-diffusion-migration conservation equations for all solution species). In this way, the potential and concentration fields were obtained in the diffusion layer, whose thickness ($5 \mu\text{m}$) corresponded to the average mass-transfer coefficient associated with experiments carried out in the impinging jet cell described above. The fluxes of all species at the solid-liquid interface are required as boundary conditions for the continuum code. DASPCK with adaptive time-stepping was used in the time integration³⁸ to deal with stiffness.

Whereas the KMC code is well-suited for the simulation of surface roughness evolution for comparison with experimental data, the

code was found to be computationally expensive, due mainly to the presence of extremely fast events associated with surface diffusion (time step $\sim 1 \text{ ns}$). In addition, it was found that the stochastic noise associated with the fluxes obtained from the KMC code adversely affected accuracy and stability of the linked codes. Therefore, instead of periodically sending fluxes from the KMC code back to the continuum equations as was done in previous multiscale models,¹³ the procedure used in the present study was as follows: (i) solve the continuum transport equations simultaneously with a set of species balance equations for the surface (listed in Table II, and (ii) create a file of the time-dependent surface concentrations and potential which was read by the KMC code in order to simulate roughness evolution. This approach is applicable because the surface reactions were first-order in the surface species, and the rates of such reactions are not functions of the degree of intermixing of species on the surface.³⁹ The time steps for the file (ii) were set much smaller ($< 20 \text{ ms}$) than the dynamic variation in the potential and surface concentrations.

Figure 2 shows two examples comparing fluxes computed by the two methods. It may be seen that the continuum surface reaction equations compute more accurate fluxes than the KMC code, whose outputs are stochastic. The relative magnitudes of fluctuations in the fluxes in the KMC results are higher when the fluxes are small.

Parameter sensitivity analysis.— Sensitivity analysis reduces the computational demand by focusing effort on the key parameters with the strongest effect on the simulation outputs, which must be determined most accurately to obtain a predictive model.^{40,41} The sensitivities were normalized in order to compare sensitivities when model outputs and parameter values may vary by orders of magnitude.⁴² The normalized sensitivity of model output y_m to the parameter β_i is defined as

$$S(y_m, \beta_i) = \frac{dy_m}{d \ln \beta_i} = \beta_i \frac{dy_m}{d\beta_i} \quad [1]$$

In this study, y_m represents a point on the current density profile or surface roughness profile. The central difference approximation of the derivative term was computed

Table III. Packing density of the surface species in the KMC simulation.

Surface species	Diameter (Å)	Packing density (no./mesoparticle)
Cu	2.54	23651.2
CuCl	2.54	23651.2
CuClPEG	16.06	591.3
Cu(I)thiolate	2.54	23651.2
Cu(I)HIT	2.54	23651.2

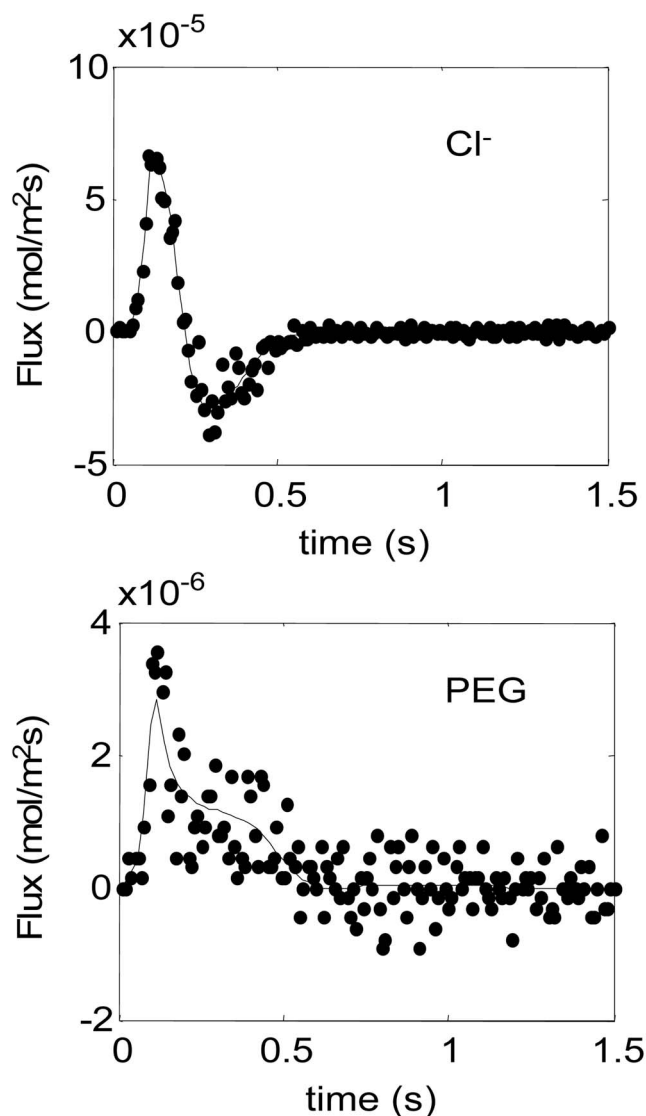


Figure 2. Comparison of the chloride_{aq} and PEG_{aq} fluxes computed from the continuum code and the KMC code, for some typical conditions, where the solid lines are the fluxes obtained from the continuum code with species balance equations and the data point are fluxes obtained from the KMC code based on concentration/potential data provided by the continuum equations. The relative fluctuations in the fluxes from the KMC code are higher when the fluxes are small, motivating the use of continuum surface reaction equations for computing the fluxes for the bulk solution equations. A detailed verification of the KMC and continuum codes is available in a thesis.³⁷

$$S(y_m, \beta_i) \approx \beta_i \left(\frac{y_m[(1 + \Delta\beta_i)\beta_i] - y_m[(1 - \Delta\beta_i)\beta_i]}{2\beta_i\Delta\beta_i} \right) = \frac{y_m[(1 + \Delta\beta_i)\beta_i] - y_m[(1 - \Delta\beta_i)\beta_i]}{2\Delta\beta_i} \quad [2]$$

Because the main purpose of the parameter sensitivity calculations was to identify which parameters to estimate based on time- and spatial-varying data, the sensitivities were averaged over the total number of points used to parameterize the time and spatial variations over all experiments

$$\text{Current density} \quad \bar{S}(i, \beta_i) = \sqrt{\frac{1}{n_d} \sum_l \sum_m S[i_l(t_m), \beta_i]^2} \quad [3]$$

$$\text{Surface roughness} \quad \bar{S}(H, \beta_i) = \sqrt{\frac{1}{n_d} \sum_l \sum_m \sum_k S[H_l(r_{H,k}; t_m), \beta_i]^2} \quad [4]$$

Appendix A contains a detailed description of the computation of the surface roughness as a function of length scale.

To suppress the effect of the stochastic fluctuations in the KMC simulation outputs on the sensitivity calculations, all KMC simulations used the same seed number.⁴³ While this introduces a bias in the sensitivity estimates, the calculated sensitivities are more accurate because the bias is small compared to the noise cancellation that results from using the same seed number.⁴⁴ Furthermore, the fixed seed simulation approach significantly reduces the number of computations required.

Parameter estimation.— Parameter estimation was used to determine optimal values for the most sensitive parameters so that the simulation outputs are closest to the experimental values. The hypothesized mechanism in Table II contains 23 unknown parameters that appear in Reactions 1-15 (i.e., 14 k_j 's, 6 α_j 's, D_s , E_a , and E_{swb}). Due to the large number of unknown parameters, only the most sensitive parameters on the measured process variables were estimated, while the remaining parameters were inferred from the related studies found in the literature. The model parameters were estimated by fitting simulation outputs to experimental current density-time data measured over the entire deposition period,⁶ and AFM roughness data at seven distinct deposition times (2, 5, 25, 50, 75, 100, and 150 s). At each deposition time, 7–8 AFM data sets were used to generate the mean roughness profile. The algorithm used to transform two-dimensional (2D) morphology data into a size-varying rms roughness is given in the Appendix A, and a discussion of this algorithm as a measure of surface roughness is available.²⁰ Of the 36 sets of experimental data that were obtained (Table I), five data sets (4, 13, 14, 27, and 28) exhibited oscillations in the potential response and were not used.

It was found that a typical run of the KMC simulation took between a day to a week or more, depending on the parameters used in the simulation. Values that increase the surface diffusion rate served to prolong the simulation time, because the internal KMC time increment varies inversely with the sum of all rates.¹¹ Here, an iterative low-order model-based parameter estimation procedure was implemented that requires fewer simulation runs than conventional parameter estimation procedures.⁴⁵ The key to reducing the computational cost is to perform parameter estimation using a low-order model that maps the key parameters to the simulation outputs. Figure 3 illustrates the following steps of the multistep parameter estimation procedure:

1. Select initial parameter estimates (in this paper, the initial parameter estimates was obtained from Part I).¹³
2. Based on sensitivities computed for each unknown parameter, define a region Y^k around the vector β^k of key parameter estimates in which the multiscale simulation model will be approximated by a low-order model between the key parameters and simulation outputs, where the superscript k refers to the iteration index for the parameter estimation procedure. Apply D-optimal design⁴⁵ to select an optimal set of N perturbed key parameter vectors on the boundary of Y^k , i.e., $\{\beta^{k,1}, \dots, \beta^{k,N}\}$.
3. Perform N runs of the full-scale multiscale simulation corresponding to the N vectors chosen in step 2. These multiscale simulations can be run in parallel.
4. Fit a low-order model between the key parameters and each simulation output (e.g., surface roughness) from the simulation re-

⁶ Although the current density is essentially constant in the galvanostatic conditions of the experiments, the current density is a good variable for fitting because it is a strong function of many of the unknown parameters, as seen in the Results section.

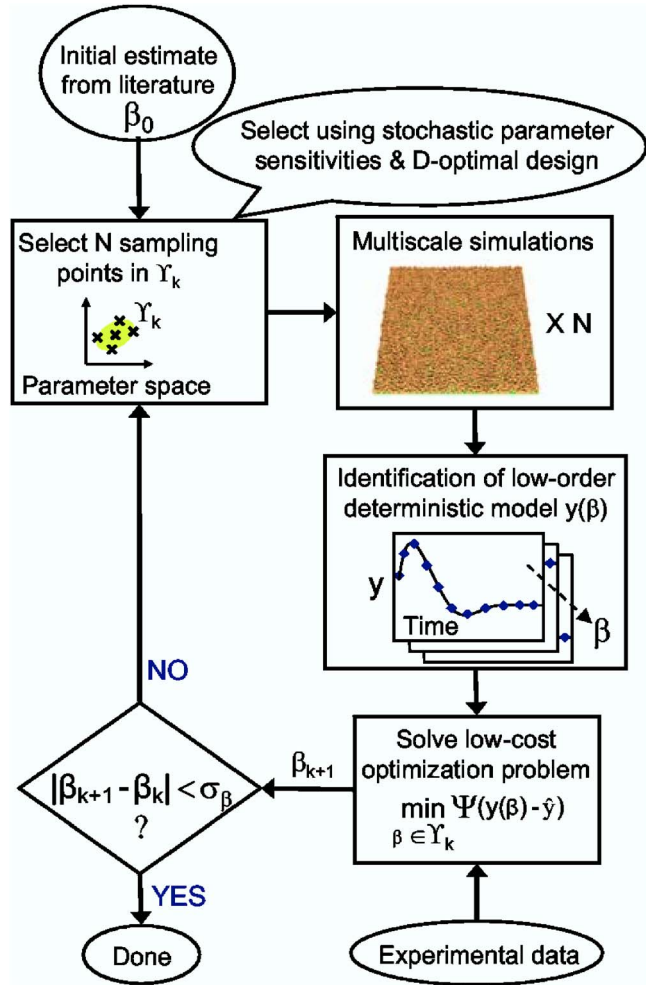


Figure 3. (Color online) Multistep parameter estimation procedure developed for simulation models that are computationally expensive and have stochastic outputs.

sults of step 3 (see Appendix B for details on the least-squares fitting procedure).

5. Compute an improved estimate β^{k+1} by minimizing the sum of squared prediction errors

$$\Psi = \min_{\beta^{k+1} \in Y^k} \sum_{i=1}^{n_p} \sum_{j=1}^{M_i} w_{i,j} (y_{i,j} - \hat{y}_{i,j})^2 \quad [5]$$

so as to match the surface roughness and current density between the experiments and model. If the optimization algorithm converges to a vector on the boundary of Y^k , then proceed to step 2. Otherwise, check whether the convergence tolerance is satisfied. If the parameter estimates are not converged, then perform another iteration in which a smaller subdomain Y^{k+1} is defined so that the identified low-order model can capture the simulation dynamics more accurately around β^{k+1} . If several iterations fail to improve the fit to the data (that is, the value of Ψ), then the parameter estimation procedure is terminated.

Whenever possible, the development of the low-order model in step 4 should be physics-motivated to improve the accuracy of the low-order representation over the parameter domain. In principle, using a physics-motivated low-order model can reduce the number of iterations required to converge to optimal parameter values, which reduces the overall computation cost for parameter estimation. In the event that such a model is not available, then a low-order

polynomial can be used⁴⁰ in which case the parameter estimation algorithm is closely related to the response surface methodology for optimization based on noisy data.⁴⁶ Because the continuum code runs quickly and is deterministic, only the KMC model was fit to a low-order model in step 4. Each surface roughness value was modeled with a quadratic equation, which is the typical polynomial used in response surface methodology.⁴⁰

Reporting the uncertainty in the optimal parameter estimates is critically important, as the uncertainty magnitude indicates how well a model is capable of predicting the process dynamics within operating constraints. Two statistical methods for estimating the parameter uncertainty are applied in this paper. The first method linearizes the model around the vector of optimal parameter estimates β^* ⁴⁵

$$\tilde{Y}_i(\beta, \mathbf{v}) \approx Y_i(\beta^*, \mathbf{v}) + F_i(\beta^*)(\beta - \beta^*) \quad [6]$$

where F_i is the Jacobian computed at β^*

$$F_i = \left. \frac{\partial \tilde{Y}_i}{\partial \beta} \right|_{\beta^*} \quad [7]$$

which was calculated using central differences. The parameter covariance matrix V_β for the linearized problem is given by⁴⁵

$$V_\beta^{-1} = \sum_{i=1}^{n_p} F_i^T V_{y,i}^{-1} F_i \quad [8]$$

Suppose that $(\hat{Y}_i - \tilde{Y}_i)$ can be approximated by a joint Gaussian distribution, then the approximate 100(1 - κ)% confidence region is the hyperellipsoid

$$(\beta - \beta^*)^T V_\beta^{-1} (\beta - \beta^*) \leq \chi_{N_\beta-1}^2(\kappa) \quad [9]$$

Although this confidence hyperellipsoid takes into account correlations in the parameter uncertainties, the confidence interval for each parameter

$$\beta_i^* - t_{1-\kappa/2}(n_d - N_\beta) \sqrt{V_{\beta,ii}} \leq \beta_i \leq \beta_i^* + t_{1-\kappa/2}(n_d - N_\beta) \sqrt{V_{\beta,ii}} \quad [10]$$

is reported in this paper because it is easier to interpret.

For the application in this paper, the total number of data points $n_d = 31 \times (1500 + 29 \times 7)$, which represents 31 experiments \times (1500 current density data points + 29 rms surface roughness for each deposition time \times 7 deposition times). However, the differences between the model and experimental values in Eq. 5 are correlated within each experimental condition, hence, such a large value for n_d is not representative of the number of independent degrees of freedom, and using such a large value of n_d in the uncertainty analysis would result in confidence intervals that are much smaller than justified by the data.^{14,47} To obtain more reasonable estimates for the parameter uncertainties which take into account the lower degrees of freedom as well as account for some of the effects of model bias, the confidence interval width in Eq. 10 was scaled by $\sqrt{(1500 + 29 \times 7)/(20 + 10 \times 7)}$, in which the 20 and 10 are estimates of the number of independent data points required to capture the time variation in potential and rms surface roughness as a function of length scale for the 31 experiments used in the parameter estimation, respectively.

The second method for quantifying uncertainty utilizes a likelihood ratio

$$\frac{(n_d - N_\beta) [\Psi(\beta) - \Psi^*]}{N_\beta \Psi^*} \approx F_{1-\kappa}(N_\beta, n_d - N_\beta) \quad [11]$$

In this study n_d was set to $31 \times (20 + 70)$, in which the 20 and 70 are estimates of the number of independent data points required to capture the time variation in applied potential and time and spatial variation in rms surface roughness for the 31 experiments used in the parameter estimation. Rearranging the above equation for Ψ gives

Table IV. Normalized sensitivities for the rate constants and transfer coefficients.

Rxn	$\bar{S}(i, k_j)$	$\bar{S}(i, \alpha_j)$	$\bar{S}(H, k_j)$	$\bar{S}(H, \alpha_j)$
1	4.9×10^{-3}	1.4×10^{-4}	130	50.0
2	3.2×10^{-4}	3.7×10^{-4}	37.0	430
3	1.9×10^{-4}	3.7×10^{-4}	17.0	430
5	3.0×10^{-3}	—	150	—
6	3.5×10^{-3}	—	14.0	—
7	1.5×10^{-4}	1.5×10^{-5}	3.4	3.4
8	3.1×10^{-3}	—	140	—
9	3.3×10^{-3}	—	8.4	—
10	3.6×10^{-3}	3.5×10^{-3}	30.0	240
11	7.6×10^{-4}	—	29.0	—
12	1.4×10^{-4}	—	5.1	—
13	2.5×10^{-3}	3.2×10^{-3}	50.0	610
14	2.1×10^{-3}	—	36.0	—
15	1.6×10^{-4}	2.0×10^{-5}	6.1	14.0

Normalized sensitivities for surface diffusion coefficient and energy barriers of copper

Rxn	$\bar{S}(H, D_s)$	$\bar{S}(H, E_a)$	$\bar{S}(H, E_{swb})$
4	2.9	3.3	6.0

$$\Psi \approx \left(1 + \frac{N_\beta F_{1-\kappa} (N_\beta n_d - N_\beta)}{n_d - N_\beta} \right) \Psi^* \quad [12]$$

In this approach, the uncertainty for the parameter is estimated by perturbing the nominal value up and down until Eq. 12 was satisfied or a physical bound on the parameter was reached. The likelihood ratio takes into account nonlinearity in the model but is much more computationally expensive than the t statistic, Eq. 10.

The above procedures were developed for extracting mechanistic information on complex additive systems for which direct measurement of individual reaction rates is difficult or impossible. This applies to the hypothesized mechanism in Table II, for which estimates of most of the kinetic parameters have not been reported or have been reported but whose accuracies are unknown. These procedures were not developed for the measurement of single reaction parameters in highly simplified systems. Also, for systems in which estimates of most of the kinetic parameters and estimates of their accuracies are available, Bayesian estimation techniques^{14,48} can be applied to utilize this information when using new experimental data to produce improved estimates.

Computer system.—All simulations were run at the National Center for Supercomputing Applications (University of Illinois, Urbana) on a Dell Xeon Linux cluster (1280 compute nodes, Intel Xeon 3.2 GHz, 12.8 Gflops single precision). Each simulation was run on a single processor. Parameter sensitivity and parameter estimation evaluations required about 60 and 2100 runs, respectively. The simulation time varied widely, from a 2–150 h per run, with longer simulation time needed for mechanisms with faster time scales. Typical minimum requirements for a parameter sensitivity evaluation plus three parameter estimation iterations were 14,000 and 400,000 CPU hours, respectively.

Results and Discussion

Parameter sensitivity results.—Table IV lists normalized sensitivities of the current density (i) and surface roughness (H) with respect to each of the model parameters. The relative magnitude of the values in each column indicates the relative sensitivities for that set. It may be seen that for each output variable some parameters are much more sensitive than others.

For example, the current density was found to be most sensitive to the reaction rate constants for Reaction 1, followed by 5, 6, 8, 9, and 10, which have similar sensitivity, and to the transfer coefficients for Reactions 10 and 13. The surface roughness was most sensitive to the rate constants for Reaction 5, followed by 8 and 1,

Table V. Initial estimates for the model parameters.

Rxn	k_j	α_j	
1	1.1×10^2 L/mol s	1/2	
2	13.0 L/mol s	1/2	
3	1.5×10^{-2} s ⁻¹	1/2	
5	5.0×10^6 L ² /mol ² s		
6	10.0 s ⁻¹		
7	1.0×10^{-2} s ⁻¹	1/2	
8	1.1×10^5 L/mol s		
9	0.7 s ⁻¹		
10	1.0 L/mol s	1/2	
11	1.0×10^6 L ² /mol ² s		
12	0.10 L/mol s		
13	21.0 L/mol s	1/2	
14	3.0×10^6 L/mol s		
15	1.5×10^5 L/mol s	1/2	
Rxn	D_s	E_a	E_{swb}
4	2×10^{-7} cm ² /s	0.30 eV	0.30 eV

which are the reactions required to adsorb Cl⁻ and then PEG to the surface, and to the transfer coefficients for Reactions 13, 2-3, and 10. That is, the current density and surface roughness were found to be sensitive to variations in the rate constant of Reaction 1, which seems intuitively reasonable because Reaction 1 is the necessary reaction step in the formation of Cu_{aq}⁺ that feeds all the subsequent deposition via Reactions 2, 5, 11, and 13. The surface roughness was found to be highly sensitive to the transfer coefficient of the reversible (electrochemical) Reactions 2-3, which is the dominant reaction path under conditions where the amount of SPS_{aq} is low. The current density was found to be highly sensitive to variation in reaction parameters in Reactions 1 and 10 (which are in the reaction pathway to form the catalyst, Cu(I)thiolate_{ads}) and also Reaction 13 (which is the catalytic reaction in which the most charge is passed under superfilling conditions when sufficient Cl_{aq}⁻ and SPS_{aq} are in solution). Also found to be sensitive were the parameters in the reversible Reactions 5-6 and 8-9, which regulate the amount of blocker, CuClPEG_{ads}, on the surface, and thus affect the current density and surface roughness for conditions for which there is sufficient Cl_{aq}⁻ and PEG_{aq} in solution.

Parameter estimation results.—Table V lists initial estimates of the values for the reaction rate constants and charge-transfer coefficients (from Table I in Part I). A sequence of iterative steps was carried out, each beginning with a set of parameter values of which the most sensitive were identified and then used to estimate improved values for use in the next iteration. A total of three iterations were carried out for the results reported below.

The measured cathodic potential from each experiment was used as input to the simulation which computed the current density, surface roughness, and concentrations of bulk and surface species. The parameter estimation could have been formulated to fit either the current density or the cathodic potential, with the alternative variable being an input to the simulation model. We chose to fit the current density, as this is a much more stringent test of the accuracy of the model predictions, because the simulation outputs are very sensitive to the cathodic potential due to the exponential dependency of the electrochemical reaction rates to potential. That is, any flaw or inaccuracy in the simulation model is magnified by using cathodic potential as input to the simulation model and using current density to quantify errors in the parameter estimation, instead of the other way around.

Figures 4 and 5 illustrate typical experimental results: a potential-time trace during constant current electrolysis, and rms surface roughness as a function of time and length scale. As an example comparison, Fig. 4b shows that the simulated and experimental current density for experiment 9 are within 15% for most of the time period, when the best-fit parameters in Table VI are used.

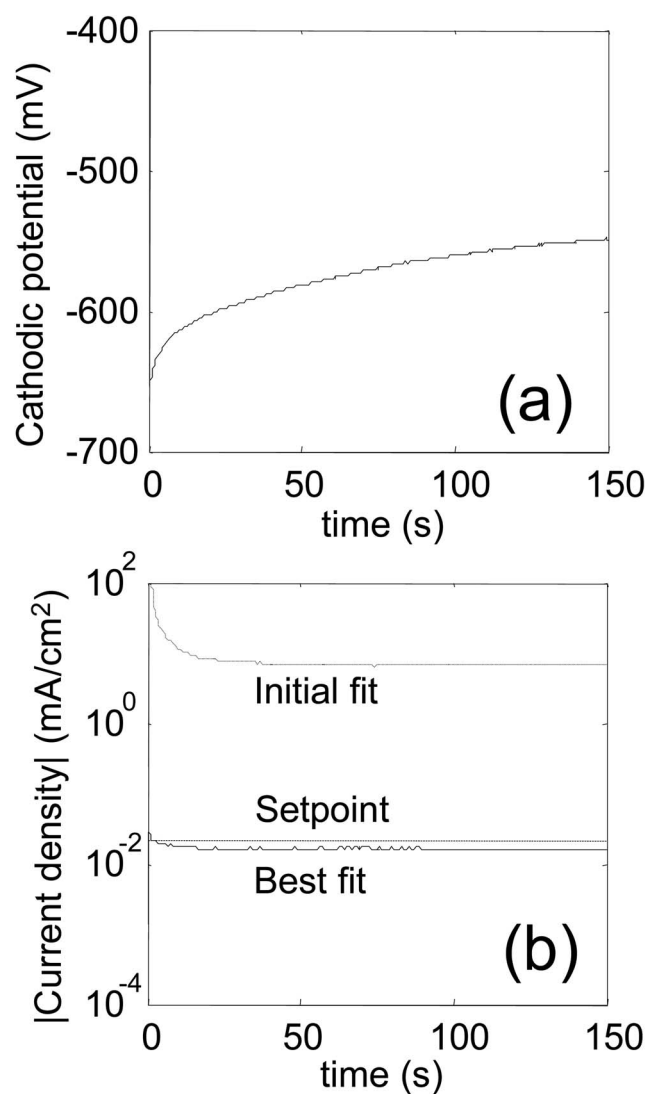


Figure 4. Potential and current response for experiment 9 under galvanostatic conditions. The bottom figure is the absolute value of the current density set point, its value computed from the simulation model using the initial parameters (Table V), and its value computed from the simulation model using parameters from the parameter estimation procedure (“best-fit,” Table VI). The spike in the cathodic potential results in a spike in the simulated current density that is not observed in the set-point current density.

For the same experiment, Fig. 5b shows the corresponding surface roughness data. With the best-fit parameters, it may be seen that the simulated results track the experimental data quite closely for longer length scales but tend to overestimate the experimental data for length scales less than $1 \mu\text{m}$, except for early in the experiment. These differences may be ascribed to reduced accuracy when a coarse-grained KMC code is used to simulate surface roughness for the shortest length scales, as discussed and quantified in some detail in a previous paper.¹¹ Not surprisingly, Fig. 4b, 5a, and b indicate that the simulation results using the parameters in Table VI fit the experimental data substantially better than when the initial parameter estimates are used (Table V). Comparisons of all of the simulated and experimental current density and rms surface roughness for the experiments are shown in Fig. 5.19–5.80 of the thesis.³⁷

From the parameter estimates reported in Table VI, it can be seen that some of the rate constants varied significantly from the initial estimates (Table V), which is not unexpected, because most of the initial parameter values were rough estimates. Reactions 7, 11, and 15 had rate constants that varied several orders of magnitude from

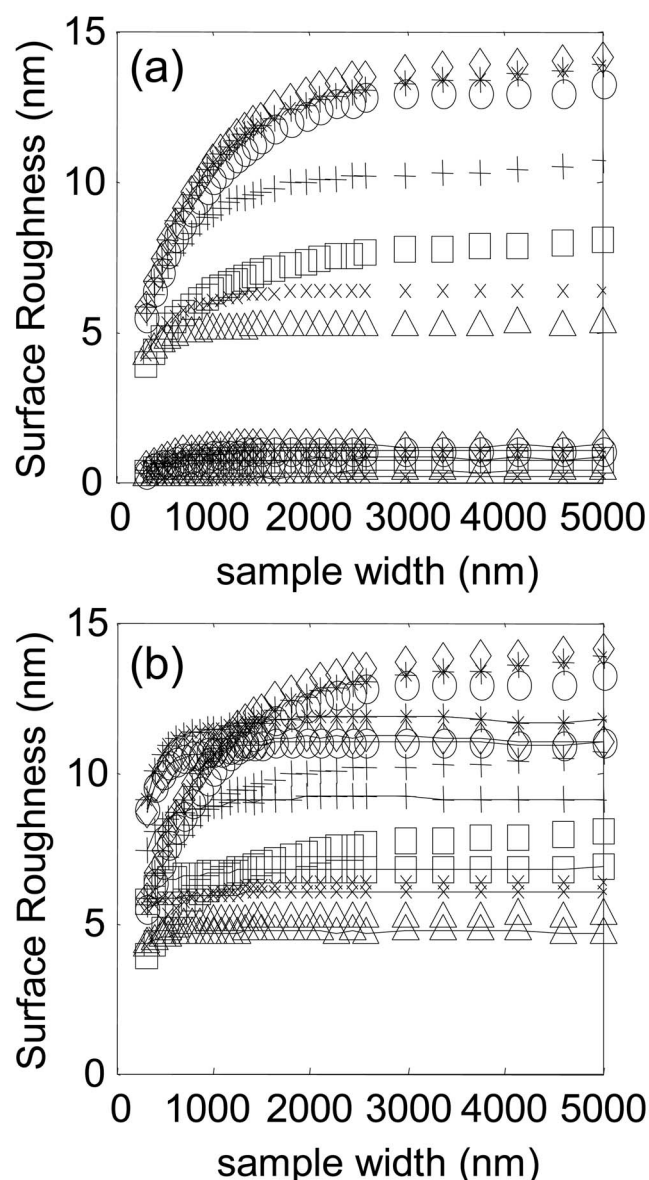


Figure 5. Surface roughness profiles for experiment 9 at 2 s (Δ), 5 s (\times), 25 s (\square), 50 s ($+$), 75 s (\circ), 100 s (\diamond), and 150 s ($*$) from the AFM images (no line) and the KMC simulation (with solid line). The KMC simulation in (a) uses the initial parameter estimates (Table V) and in (b) uses the parameters from the parameter estimation procedure (“best,” Table VI).

the initial estimates, which were all highly uncertain,¹³ and the confidence intervals determined by F statistics are very wide (Table VI), indicating that these parameters are barely identifiable, even with the rich data set collected in this study. In contrast, it can be seen that the values of transfer coefficients are fairly close to the expected theoretical and reported values of between 0.2 and 0.5.⁴⁹

The upper and lower limit on the 95% confidence interval for each parameter value are denoted in Table VI by a line below or above the variable, respectively. According to t statistics, the uncertainty in each k_j is within 20% of the nominal value, except for Reactions 3, 7, and 15, which have 26, 30, and 21% variation, respectively. Higher uncertainties for k_3 , k_7 , and k_{15} are attributed to the far less significance of the corresponding rates compared with the rates of other reactions that act on the same species, resulting in the kinetics of these reactions having a weak effect on the experimental data. For instance, Reaction 3 has a rate that is several orders of magnitude smaller than that of its reverse reaction (Reaction 2).

Table VI. Parameter estimates and 95% confidence intervals for the mechanism in Table II. Lower (upper) limits on confidence intervals are represented by a line below (above) the variable. The “ Δ ” refers to the total length of each confidence interval.

Rxn	Nominal	k_j			F statistics			Unit
		k_j	\bar{k}_j	Δk_j	k_j	\bar{k}_j	Δk_j	
1	68	65	72	7	41	90	49	L/mol s
2	13	11	16	5	0	16	16	L/mol s
3	1.0×10^{-2}	7.4×10^{-3}	1.3×10^{-2}	5.6×10^{-3}	0	12	12	1/s
5	1.5×10^7	1.3×10^7	1.6×10^7	0.3×10^7	5.2×10^6	3.1×10^7	2.6×10^7	L ² /mol ² s
6	4.1	3.6	4.5	0.9	2.1	11	9	1/s
7	3.2×10^{-9}	2.2×10^{-9}	4.1×10^{-9}	1.9×10^{-9}	0	2.8×10^{-4}	2.8×10^{-4}	1/s
8	1.0×10^5	9.1×10^4	1.1×10^5	1.9×10^4	3.1×10^4	2.0×10^5	1.7×10^5	L/mol s
9	5	4.4	5.6	1.2	2.5	17	15	1/s
10	8.0×10^{-2}	7.6×10^{-2}	8.5×10^{-2}	0.9×10^{-2}	4.7×10^{-2}	2.2×10^{-1}	1.7×10^{-1}	L/mol s
11	1.4×10^{14}	1.2×10^{14}	1.6×10^{14}	0.4×10^{14}	3.1×10^{13}	2.7×10^{16}	2.7×10^{16}	L ² /mol s
12	10	8.9	11	2	0	4.4×10^2	4.4×10^2	L/mol s
13	1.3×10^3	1.0×10^3	1.6×10^3	0.6×10^3	4.9×10^2	3.8×10^3	3.3×10^3	L/mol s
14	6.8×10^7	6.1×10^7	7.5×10^7	1.4×10^7	3.7×10^7	1.4×10^8	1.0×10^8	L/mol s
15	4.6×10^2	3.6×10^2	5.7×10^2	2.1×10^2	0	1.2×10^6	1.2×10^6	L/mol s

Rxn	Nominal	α_j			F statistics			Unit
		α_j	$\bar{\alpha}_j$	$\Delta\alpha_j$	α_j	$\bar{\alpha}_j$	$\Delta\alpha_j$	
1	0.20	0.19	0.21	0.02	0.08	0.24	0.16	—
2	0.51	0.49	0.53	0.04	0	0.66	0.66	—
7	0.50	0.34	0.66	0.32	0	1	1	—
10	0.500	0.497	0.503	0.006	0.47	0.57	0.10	—
13	0.50	0.49	0.51	0.02	0.44	0.55	0.11	—
15	0.50	0.44	0.56	0.12	0.17	0.56	0.39	—

Rxn	Nominal	D_s			F statistics			Unit
		D_s	\bar{D}_s	ΔD_s	D_s	\bar{D}_s	ΔD_s	
4	1.0×10^{-6}	7.3×10^{-7}	1.3×10^{-6}	5.7×10^{-7}	9.3×10^{-7}	1.1×10^{-6}	1.7×10^{-7}	cm ² /s

Rxn	Nominal	E_a			F statistics			Unit
		E_a	\bar{E}_a	ΔE_a	E_a	\bar{E}_a	ΔE_a	
4	31	21	41	20	29	34	5	meV

Rxn	Nominal	E_{swb}			F statistics			Unit
		E_{swb}	\bar{E}_{swb}	ΔE_{swb}	E_{swb}	\bar{E}_{swb}	ΔE_{swb}	
4	11.5	7.8	15.2	7.4	11	12	1	meV

Reaction 7 experiences a compounded effect, as its rate is not only much smaller than that of its reverse chemical counterpart reaction (Reaction 5), but also smaller than that of its competitive reaction (Reaction 8). Analogous to k_3 , Reaction 15, which decomposes Cu(I)HIT_{ads} and then releases HIT back to the solution, has a very small rate compared to Reaction 14, which consumes HIT_{aq} in order to make Cu(I)HIT_{ads}. This would be consistent with the notion that HIT affects the overall mechanism by slowly accumulating through most of the copper electroplating experiments and is significantly released only near the end of an experiment. If only a small amount of HIT dissociates during the experiments, then the experimental data will contain insufficient information to obtain a highly accurate estimate of the kinetic parameters for the HIT dissociation reaction, Reaction 15.

For the t statistics in Table VI, the subset of k_j values with the smallest uncertainty ($< \sim 10\%$) are k_1 , k_5 , k_8 , k_{10} , and k_{14} . The fact that these k_j values have smaller uncertainty indicates that the cor-

responding reactions are highly influential in the dynamics of the copper electrodeposition process. In particular, Reaction 1 is important as it forms Cu_{aq}⁺ ions, which are the precursor to Cu_{ads}, CuCl_{ads}, and Cu(I)thiolate_{ads}, of which the latter two adsorbed species are effective modifiers of the deposition rate. Reaction 5 uses Cu_{aq}⁺ to form CuCl_{ads} and subsequently, Reaction 8 transforms CuCl_{ads} to CuCIPEG_{ads}. Reactions 1, 5, and 8 are simultaneously important because they collectively form the pathway to create CuCIPEG_{ads}. The fact that these parameters can be estimated with less uncertainty supports the experimental evidence that CuCIPEG_{ads} is a strong surface site blocker for copper electrodeposition. Reaction 10 generates thiolate_{aq}⁻ from SPS_{aq} and thiolate_{aq}⁻ is the ligand of Cu(I)thiolate_{ads}, which acts as catalyst. Numerous experimental studies have suggested the influence of Cu(I)thiolate_{ads} on the potential response curve. Finally, the uncertainty analysis based on the t statistics indicates that HIT can be an effective Cu(I)thiolate_{ads} remover. This

result is in agreement with trench in-fill data which show that the deposit has a flat, smooth surface after filling a trench when HIT is present and forms bumps otherwise. The effect of HIT is manifested in the surface roughness data which were used in the parameter estimation.

Comparing the relative magnitude of the uncertainties for each α_j gives similar information on the electrochemical reactions. The small confidence intervals for most of the transfer coefficients are not unexpected, because these model parameters enter into an exponential function of the overpotential, which is input into the multi-scale simulation model to compute the current density and surface roughness. The large normalized sensitivity between the current density and the transfer coefficient for Reaction 1 (Table IV) suggests that the transfer coefficient is highly identifiable from measurements of the current density, which results in the small confidence interval on the transfer coefficient for Reaction 1. On the other side of the spectrum, the normalized sensitivities for Reaction 15 are low, and the confidence intervals are fairly large. The normalized sensitivities do not always have a perfect inverse correlation with the size of the confidence intervals; however, this is because the individual normalized sensitivities do not take into account the correlations between parameter estimates, for example, where shifts in different model parameters have a similar effect on the overall fit of the simulation outputs to the experimental data. Comparison of the magnitude of the sensitivities in Table IV with the confidence intervals in Table VI for the various reactions indicates that the correlation between these variables is fairly good for this particular application.

The likelihood ratio utilizing F statistics shows larger uncertainties for all the k_j 's and α_j 's compared to the t statistics. In principle, the likelihood ratio provides a more accurate estimation of confidence intervals, as it explicitly takes the model nonlinearity into consideration. The main reason that t statistics applied to the linearized model is more commonly used in practice⁴⁵ is that the likelihood ratio test is much more computationally expensive, as it requires many more iterations to search for the perturbation size in each parameter β_i such that the sum of squared errors Ψ is equal to a given fraction larger than its optimal value. Table VI contains zero entries for some lower bounds of k_j and α_j , indicating that those parameters do not have the lower bound that can perturb the sum of squared errors Ψ to the value dictated by the F statistics (see Eq. 12). The rate constant k_2 has zero lower bound because for a substantial portion of the 31 experiments, the fraction of $\text{Cu}_{\text{aq}}^{2+}$ consumed by Reaction 2 decreases rapidly with time compared to Reactions 5, 11, and 13. Therefore, shutting off this $\text{Cu}_{\text{aq}}^{2+}$ channel will not cause the Ψ to increase considerably. Reactions 3, 7, and 15 have very small rates for all experimental conditions, and hence, shutting these reaction pathways does not change Ψ appreciably. Reaction 12 which decomposes $\text{Cu(I)thiolate}_{\text{ads}}$ has a negligible rate compared to its competitor, which is Reaction 14, and therefore, the same reasoning for zero lower bound can be applied to this reaction. Analysis of the α_j bounds obtained by F statistics gives consistent information about the identifiability of the kinetics of each reaction in the mechanism.

The uncertainties in the surface diffusion parameters quantified by F statistics are smaller than for t statistics. The fact that all of the surface diffusion parameters have fairly small uncertainty (<10%) for the more accurate F statistics suggests that biases in the surface diffusion modeling are probably fairly small, and that the main biases in the model are associated with uncertainty in the reaction mechanism. This would agree with physical intuition, because the surface diffusion model used in this paper is fairly complete in its accounting for all nearest-neighbor and next-nearest-neighbor interactions between surface species,³⁷ whereas the hypothesized reaction mechanism involves some assumptions on surface chemistry which, by comparison, are uncertain.

While the nominal estimates of all of the transfer coefficients for electrochemical reactions are near the theoretical value of 0.5, ex-

cept for that corresponding to reduction of $\text{Cu}_{\text{aq}}^{2+}$ which was estimated at 0.2, several of these estimates had large confidence intervals, indicating that those values are uncertain. The accuracy in these transfer coefficients could be improved by carrying out experiments over a wider range of applied potential, because that would increase the effects that these transfer coefficients have on the rates of the associated reactions (see last column of Table II), which would have larger effects on the experimental data.

The large confidence intervals for the kinetic parameters for Reactions 14 and 15 indicate that future experiments should be directed toward reducing the uncertainties in the HIT reactions. This is because the goal of this reaction mechanism is for incorporation into trench-infill simulations, and the HIT reactions must be known fairly accurately in such simulations to be able to accurately predict how soon the "bump" shortly after a trench has been superfilled will be removed, or how well it will be suppressed as a function of additive concentrations. Because HIT acts on a much slower time scale than most of the rest of the chemistry, experiments designed to obtain more data on these reactions should run for a much longer time, under experimental conditions in which substantial $\text{Cu(I)thiolate}_{\text{ads}}$ covers the surface (e.g., high SPS, low PEG, and low acid) and enough HIT is added to remove $\text{Cu(I)thiolate}_{\text{ads}}$ from the surface. The reaction mechanism is sufficiently developed that model-based experimental design could be applied, which uses the reaction mechanism, its parameter estimates, and its uncertainties to design experiments to maximize the information needed to reduce the magnitude of the parameter uncertainties.⁴⁵ Such methods have been applied to other microelectronics processes to reduce uncertainties in a complex reaction mechanism.⁵⁰

Reaction mechanism.— For each of the experimental conditions listed in Table I, the estimated parameter values listed in Table VI were used to simulate the transient surface coverage of adsorbed species and the surface concentration of solution species. Of the entire set of results, which are reported in detail elsewhere,³⁷ several key results are summarized here.

For the conditions of experiment 2 (Table I), Fig. 6a shows the surface coverage of several adsorbed species as a function of time. The initial state is that all surface sites are "bare" Cu_s sites which, after the onset of electrolysis, become occupied in a stochastic manner by adsorbed species [CuCl_{ads} , $\text{CuCIPEG}_{\text{ads}}$, $\text{Cu(I)thiolate}_{\text{ads}}$, or $\text{Cu(I)HIT}_{\text{ads}}$], or else remain as unoccupied Cu_s sites. The insert shows results for short time behavior where it is seen that CuCl_{ads} increases through a maximum at 0.3 s, followed by a maximum in $\text{CuCIPEG}_{\text{ads}}$ at 1.3 s. The main part of Fig. 6a illustrates behavior at longer times where it is seen that the surface coverage by $\text{Cu(I)thiolate}_{\text{ads}}$ gradually increases, replacing previously adsorbed $\text{CuCIPEG}_{\text{ads}}$, until a nearly steady-state surface coverage at about 50 s. These findings confirm the generally accepted notion that the suppressor complex is formed more easily (kinetically) and then replaced by the more stable (thermodynamically) adsorbed accelerator complex. Also, for the conditions of experiment 2, Fig. 6b indicates how the solution concentrations at the surface vary in time for several species that participate in influencing the competitive adsorption of PEG_{aq} and $\text{Cu(I)thiolate}_{\text{aq}}$. It may be seen that PEG_{aq} becomes significantly depleted during the initial second, while free $\text{thiolate}_{\text{aq}}^-$ appears rapidly at the outset but then decreases due to formation of MPS_{aq} (Reaction 16) and complexation with $\text{Cu}_{\text{aq}}^{2+}$ (Reaction 11). These results suggest that Reactions 1 and 5 occur rapidly to produce CuCl_{ads} , followed by Reaction 8 to form $\text{CuCIPEG}_{\text{ads}}$. Under the conditions of experiment 2, PEG_{aq} adsorption via Reaction 8 is transport-controlled due to its low bulk concentration and large adsorption rate constant. The rapid initial adsorption of PEG_{aq} thus serves to occupy a significant number of the surface sites, which limits the number of unoccupied Cu_s sites where the generation of $\text{thiolate}_{\text{aq}}^-$ may occur by Reaction 10. Thus, the pathway to $\text{Cu(I)thiolate}_{\text{ads}}$ formation via Reactions 16 and 11 is impeded at first. Eventually, however, due in part to the low acid

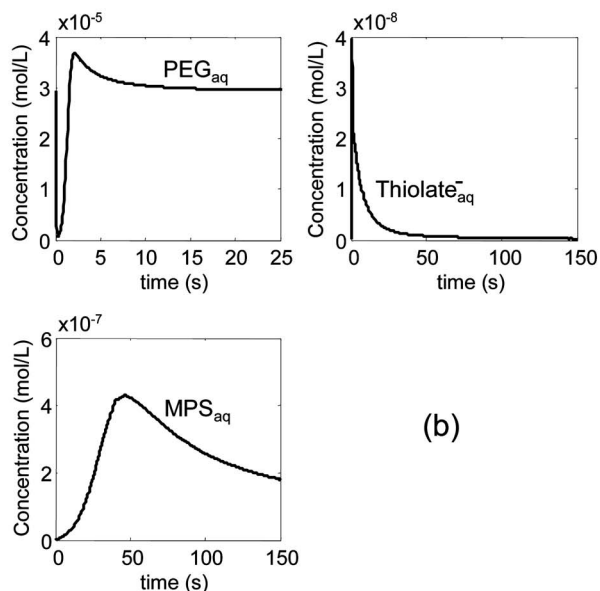
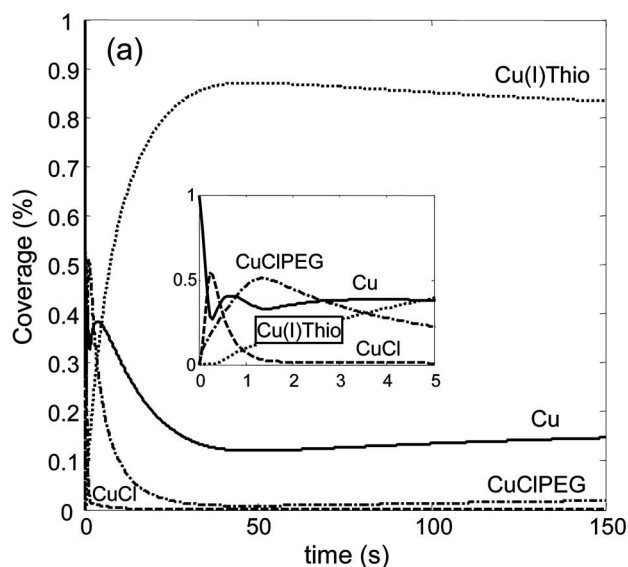


Figure 6. (a) Surface coverage by Cu_s , CuCl_{ads} , $\text{CuCIPEG}_{\text{ads}}$, and $\text{Cu(I)thiolate}_{\text{ads}}$ for experiment 2. The coverage by $\text{Cu(I)HIT}_{\text{ads}}$ is very low and therefore is not included in the above plots. (b) Concentration of PEG_{aq} , $\text{thiolate}_{\text{aq}}^-$, and MPS_{aq} at the surface as a function of time.

concentration of experiment 2, the competitive adsorption of $\text{Cu(I)thiolate}_{\text{ads}}$ is favored via the (reversible) Reactions 11-12. For these conditions the surface coverage of $\text{Cu(I)HIT}_{\text{ads}}$ was negligible ($\sim 10^{-4}$).

The conditions for experiment 3 correspond to low SPS and high acid concentrations (see Table II). The numerical results provided in Fig. 7 illustrate that the surface coverage by $\text{CuCIPEG}_{\text{ads}}$ remains higher than for experiment 2. These results are consistent with the interpretation that: (i) the low SPS concentration in experiment 3 results in low $\text{thiolate}_{\text{aq}}^-$ by Reaction 10, low MPS_{aq} by Reaction 16, and low formation of $\text{Cu(I)thiolate}_{\text{ads}}$ by Reaction 11; and (ii) the high acid concentration in experiment 3 shifts Reaction 12 to the right so that any $\text{Cu(I)thiolate}_{\text{ads}}$ that forms tends to desorb back into the bulk solution. Both effects reduce the rate of $\text{Cu(I)thiolate}_{\text{ads}}$ production and increase the kinetics of its consumption with the result that sites initially occupied by $\text{CuCIPEG}_{\text{ads}}$ do not become significantly displaced by $\text{Cu(I)thiolate}_{\text{ads}}$.

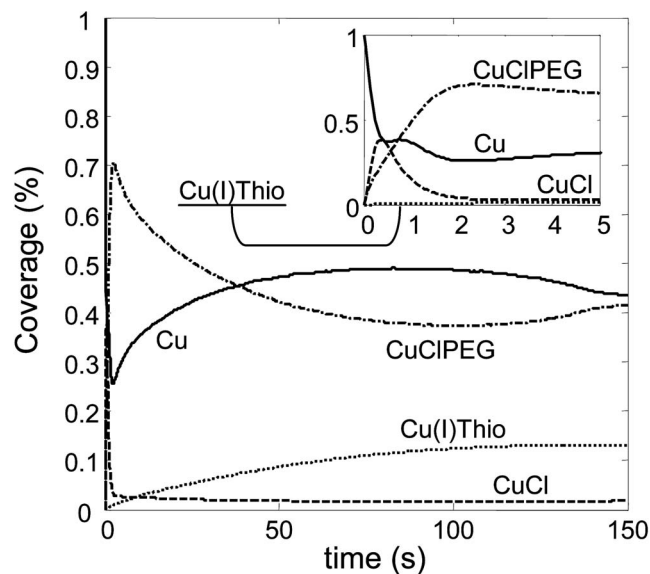


Figure 7. Surface coverage by Cu_s , CuCl_{ads} , $\text{CuCIPEG}_{\text{ads}}$, and $\text{Cu(I)thiolate}_{\text{ads}}$ for experiment 3. The coverage by $\text{Cu(I)HIT}_{\text{ads}}$ is very low and therefore is not included in the above plots.

Additional results, available elsewhere,³⁷ indicated that for the conditions of experiment 5, where acid, SPS_{aq} , and PEG_{aq} concentrations are high, the simulated coverage of $\text{CuCIPEG}_{\text{ads}}$ quickly increased and remained high throughout deposition. As was found in experiment 3, the high acid concentration resulted in fast kinetics for the consumption of $\text{Cu(I)thiolate}_{\text{ads}}$, in which case $\text{CuCIPEG}_{\text{ads}}$ was not displaced from the surface. However, the higher value of SPS for experiment 5 compared to experiment 3 did not produce enough MPS_{aq} to drive Reaction 11 to the right to form $\text{Cu(I)thiolate}_{\text{ads}}$.

For experiment 7, both SPS_{aq} and acid concentrations are low. The simulations indicated that $\text{Cu(I)thiolate}_{\text{ads}}$ can gradually replace $\text{CuCIPEG}_{\text{ads}}$, even under conditions where the SPS_{aq} concentration is much lower than in the conditions of experiment 5. These results are consistent with the view that a low acid concentration favors formation of $\text{Cu(I)thiolate}_{\text{ads}}$ due to reversible Reactions 11-12.

The effect of chloride was investigated with simulations for the conditions of experiments 9, 16, and 18. The numerical results for experiment 9 indicated that, even when the acid concentration is high, $\text{Cu(I)thiolate}_{\text{ads}}$ gradually replaced $\text{CuCIPEG}_{\text{ads}}$ if both initial Cl_{aq}^- and PEG_{aq} concentrations are low, because then the reversible Reactions 5-6 and 8-9 are unfavorable for $\text{CuCIPEG}_{\text{ads}}$ at longer times. If the Cl_{aq}^- concentration is high (experiment 16), then $\text{CuCIPEG}_{\text{ads}}$ coverage remains high during electrodeposition, even in the presence of high SPS_{aq} concentration and low HIT_{aq} concentration, because high Cl_{aq}^- concentration shifts Reaction 5, and subsequently, Reaction 8, to the right. If the Cl_{aq}^- concentration is low (experiment 18), it was found that $\text{CuCIPEG}_{\text{ads}}$ coverage dropped gradually from a high value while $\text{Cu(I)thiolate}_{\text{aq}}$ coverage increased steadily, even with a low SPS_{aq} and high HIT_{aq} concentration; the low Cl_{aq}^- concentration resulted in Reactions 5-6 and 8-9 being unfavorable for $\text{CuCIPEG}_{\text{ads}}$ at longer times. Simulations for the conditions of experiments 10 and 12 showed similar trends.³⁷

The effect of current density was investigated for the conditions of experiments 34 and 35. High current density resulted in low Cu_{aq}^+ concentration near the surface, with the consequence that formation of both $\text{CuCIPEG}_{\text{ads}}$ and $\text{Cu(I)thiolate}_{\text{ads}}$ was less favorable, and the surface exhibited a high coverage of "bare" Cu_s sites. These results support the observation that additives are more active at low overpotentials.⁴

Conclusion

The simulation results reported here are based on a hypothesized mechanism (Table II) along with experimental data. This work addresses the procedures for identifying the most sensitive parameters and estimating their values and confidence intervals based on that hypothesis. Not addressed here is whether there might be other species or other reactions, or how to select from among multiple reasonable hypotheses, or how to design additional experiments to maximize the information needed to reduce the parameter uncertainties in complex reaction mechanisms. Readers interested in techniques for addressing these problems are referred to recent review papers.^{16,51}

A multistep parameter estimation procedure was implemented to estimate the kinetic parameters of a mechanism for additive-mediated copper electrodeposition. The procedure reduces computational time by employing in the optimization a low-order model determined by input-output identification on the multiscale simulation model. The multiscale model utilized a coupling strategy for the continuum and (2 + 1)D kinetic Monte Carlo codes which gave higher numerical accuracy compared to any existing coupling strategy by isolating the noisy KMC simulation outputs. The parameter estimation algorithm was used to analyze AFM images and applied potential data collected from a high-throughput experimental system that investigated a D-optimal operating space for seven process input variables.

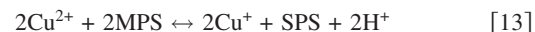
Sensitivity analysis indicated (Table IV) that the current density was most sensitive to the reaction rate constant k_1 followed by k_5 , k_6 , k_8 , k_9 , and k_{10} , and also to the transfer coefficients α_{10} and α_{13} . The surface roughness was most sensitive to rate constant k_5 , followed by k_8 and k_1 , and to the transfer coefficients α_{13} , α_2 ($\alpha_3 = 1 - \alpha_2$), and α_{10} . These results seem reasonable because these reactions comprise the formation of Cu_{aq}^+ , which feeds all four deposition routes, as well as the formation of the $\text{CuCIPEG}_{\text{ads}}$ suppressor, which competes for surface sites with $\text{Cu(I)thiolate}_{\text{ads}}$.

The parameter estimation procedure significantly improved the fit between the simulation predictions and the experimental data (Table VI) when compared to the initial estimates (Table V) and recently¹³ by a combination of literature data, intuition, and simple current-voltage experiments. The reaction rates having the smallest uncertainty (Table VI) were found to be k_1 , k_5 , k_8 , k_{10} , and k_{14} . The fact that these k_j values are also the most sensitive indicates that the corresponding reactions are highly influential in the dynamics of the copper electrodeposition process. These results are in agreement with numerous experimental reports that $\text{CuCIPEG}_{\text{ads}}$ is a strong surface site blocker for copper electrodeposition, and that $\text{Cu(I)thiolate}_{\text{ads}}$ acts as catalyst.

By using the estimates for parameter values to predict the dynamics of surface coverage by reaction intermediates (Fig. 6 and 7), it was found that due to its large adsorption rate constant, $\text{CuCIPEG}_{\text{ads}}$ coverage tends toward high values soon after the potential is applied; the relative initial coverage depending mostly on initial PEG concentration. As deposition proceeds, subsequent $\text{CuCIPEG}_{\text{ads}}$ behavior depends strongly on the Cl_{aq}^- concentration, which can shift the CuCIPEG adsorption equilibrium. Due to the high initial coverage of reactive sites by $\text{CuCIPEG}_{\text{ads}}$, the rate of SPS reduction is initially limited by surface kinetics. The initial value of SPS concentration does not dramatically affect $\text{Cu(I)thiolate}_{\text{ads}}$ coverage, which is always low at the beginning. Subsequently, the building up of $\text{Cu(I)thiolate}_{\text{ads}}$ depends mainly on acid concentration. Low acid concentration favors Cu(I)thiolate adsorption, which enables $\text{Cu(I)thiolate}_{\text{ads}}$ to replace $\text{CuCIPEG}_{\text{ads}}$, provided that Cl_{aq}^- concentration is not too high. A high current density results in a lower Cu_{aq}^+ concentration, which decreases the coverage of both $\text{CuCIPEG}_{\text{ads}}$ and $\text{Cu(I)thiolate}_{\text{ads}}$.

The extent to which the foregoing conclusions support what is known about the additive effects represents a test of the hypothesized mechanism. Progress is made by following the scientific

method of repeatedly modifying the hypothesis and making additional observations, while using numerical simulations to evaluate the consequences.⁵² The identification of the most sensitive reactions serves to guide where improvements in the hypothesis would have a significant effect. For example, the MPS concentration near the surface should be important because it influences catalyst $\text{Cu(I)thiolate}_{\text{ads}}$ formation via Reaction 11. The hypothesized mechanism does not include the equilibrium reaction



which would require the reverse of Reaction 10, in addition to equilibration among Reactions 1, 11, 12, and 16. Sensitivity analysis could be applied to a mechanism with these revisions to assess the magnitude of the effect this modification has on the current density and surface roughness. An additional example would be to take into consideration the transient buildup of breakdown- and side-products which influence additive behavior, or to include the presence of oxygen. These and other refinements to the hypothesis, however, could in principle be developed with the same general procedures described in this work.

The methods reported here are flexible and portable, and can be applied to other applications beyond the copper electrodeposition system used here in its initial development. The features that are common to many such applications are (i) predictive models are required for engineering decision-making (ii) scientific understanding is uncertain, although multiple reasonable hypotheses of mechanistic behavior are available (iii) critical events are difficult to observe directly by experiment and (iv) the problem spans from molecular details of surface chemistry and structure formation to macroscopic aspects of transport processes and reactor conditions.

Acknowledgments

The authors express heartfelt thanks to the late Dr. Andricacos for his contribution to this paper. Funding for this work was provided by the IBM Corporation and the National Science Foundation under grants CTS-0135621, EHR-0426328, CTS-0438356, as well as for computing resources under NRAC MCA-01S022 (via the National Center for Supercomputing Applications, University of Illinois, Urbana). Any opinions, findings, and conclusions or recommendations expressed in this material are those of the authors and do not necessarily reflect the views of the National Science Foundation.

University of Illinois at Urbana-Champaign assisted in meeting the publication costs of this article.

Appendix A Surface Roughness

A 128×128 KMC grid was chosen to simulate the evolution of surface roughness on a $5 \times 5 \mu\text{m}$ region. For this application, these 2D grid dimensions gave the best tradeoff between minimizing computation cost and adequately resolving the surface structures observed on the AFM images. As a result, each AFM image was coarsened by averaging each 4×4 grid of measurements before the data was subject to the surface roughness calculation.

The surface roughness quantifies how the averaged height variation changes for various distances between points on the surface. With no loss of generality, the point of reference was taken to be one of the four corners of the electrodeposited plate. The algorithm for computing surface roughness is:

```

A. Create distance arrays, i.e.,  $aa$  and  $r_H$  (where "floor" means to truncate the decimal places)
Initialization:  $a = 8$ ,  $a_{\text{step}} = 10$ ,  $ii = 1$ 
Loop to create  $aa$  and  $r_H$ :
  While ( $a < 128$ ),
     $aa[ii] = a$ 
    If ( $a \leq 36$ ), then  $a = a + 2$ ,
    ElseIf ( $a \leq 64$ ), then  $a = a + 4$ ,
    ElseIf ( $a \leq 104$ ), then  $a = a + 10$ ,
    Else  $a_{\text{step}} = \text{floor}(1.2 \times a_{\text{step}})$ ,  $a = a + a_{\text{step}}$ ,
  EndIf
   $ii = ii + 1$ 
End While

```

$$aa[ii] = 128;$$

$$r_H = aa \times 5000/128$$

Compute the surface roughness (where “dim” is the dimension of the vector argument)

B. Loop to compute rms roughness: H

$$n_{aa} = \text{dim}(aa)$$

For $ii = 1:n_{aa} - 1$,

$$nn = 0, HH = 0,$$

For $jj = 1:8:(128 - aa[ii])$, %jj is incremented by eight each time

For $kk = 1:8:(128 - aa[ii])$, %kk is incremented by eight each time

$$nn = nn + 1,$$

$$d_i = d[kk:kk + aa[ii] - 1, jj:jj + aa[ii] - 1],$$

$$\bar{d}_i = \frac{1}{aa(ii)^2} \sum_{iii=1}^{aa(ii)} \sum_{jjj=1}^{aa(ii)} d_i(iii, jjj),$$

$$HH(nn) = \sqrt{\frac{1}{aa(ii)^2} \sum_{iii=1}^{aa(ii)} \sum_{jjj=1}^{aa(ii)} (\bar{d}_i - d_i(iii, jjj))^2} \times scl$$

End loop over kk

End loop over jj

$$H(ii) = \frac{1}{nn} \sum_{iii=1}^{nn} HH(iii)$$

End loop over ii

$$\bar{d} = \frac{1}{aa(n_{aa})^2} \sum_{iii=1}^{aa(n_{aa})} \sum_{jjj=1}^{aa(n_{aa})} d(iii, jjj)$$

$$H(n_{aa}) = \frac{1}{aa(n_{aa})^2} \sum_{iii=1}^{aa(n_{aa})} \sum_{jjj=1}^{aa(n_{aa})} (\bar{d} - d(iii, jjj))^2$$

In this algorithm, scl is the equipment scaling factor, d is a 2D array of dimension 128×128 , and the colon notation represents selection of a range of integer values. For instance, $aa[1:3] = [aa[1] \ aa[2] \ aa[3]]$.

Appendix B

Fitting Low-Order Model in Step 4 of Multistep Parameter Estimation

The low-order model fit in step 4 of the multistep parameter estimation procedure has the form

$$y_m = p_0^m + \sum_{j=1}^M p_j^m \tilde{\beta}_j + \sum_{k=1}^M \sum_{l \geq k}^M p_{k,l}^m \tilde{\beta}_k \tilde{\beta}_l \quad [\text{B-1}]$$

where y_m represents the m th target point on a surface roughness profile, M is the number of key parameters, each p^m with a subscript is a coefficient in the polynomial, and each $\tilde{\beta}_j$ is a normalized key parameter, defined by the following relations⁴⁰

$$\tilde{\beta}_j = \frac{\ln(\beta_j^k / \beta_{0j})}{\ln f_j} \quad [\text{B-2}]$$

$$f_j = \sqrt{\frac{\beta_{\max,j}^k}{\beta_{\min,j}^k}} \quad [\text{B-3}]$$

$$\beta_{0j} = \sqrt{\beta_{\max,j}^k \beta_{\min,j}^k} \quad [\text{B-4}]$$

In the above equations, $\beta_{\max,j}^k$ and $\beta_{\min,j}^k$ are the maximum and minimum of the key parameter β_j^k . The normalization step maps the upper and lower bounds of β_j^k to +1 and -1 respectively. The quadratic equations written for N simulation data sets can be stacked into vector form

$$Y_m = B p^m \quad [\text{B-5}]$$

where

$$Y_m = [y_m(\beta^{k,1}) \ \dots \ y_m(\beta^{k,N})]^T \quad [\text{B-6}]$$

$$B = \begin{bmatrix} 1 & \tilde{\beta}_1^1 & \dots & \tilde{\beta}_M^1 & \tilde{\beta}_1^1 \tilde{\beta}_1^1 & \tilde{\beta}_1^1 \tilde{\beta}_2^1 & \dots & \tilde{\beta}_M^1 \tilde{\beta}_M^1 \\ \vdots & \vdots & \ddots & \vdots & \vdots & \vdots & \ddots & \vdots \\ 1 & \tilde{\beta}_1^N & \dots & \tilde{\beta}_M^N & \tilde{\beta}_1^N \tilde{\beta}_1^N & \tilde{\beta}_1^N \tilde{\beta}_2^N & \dots & \tilde{\beta}_M^N \tilde{\beta}_M^N \end{bmatrix} \quad [\text{B-7}]$$

$$p^m = [p_0^m \ p_1^m \ \dots \ p_M^m \ p_{1,1}^m \ p_{1,2}^m \ \dots \ p_{M,M}^m]^T \quad [\text{B-8}]$$

where the superscript on $\tilde{\beta}$ refers to the index of parameter sets in step 2. It is easy to show that for p^m to have a unique solution, $N \geq [1 + M + M(M + 1)/2]$. If B is a full column rank, then the vector of regression coefficients p^m is given by $p^m = (B^T B)^{-1} B^T Y_m$.

List of Symbols

B	factorial design matrix
D_s	surface diffusion coefficient of copper, cm^2/s
E_a	diffusion energy barrier for breaking one face, eV
E_{swb}	Ehrlich-Schwoebel energy barrier, eV
F	Faraday's constant, $9.65 \times 10^4 \text{C/equiv}$
$F_{1-\kappa}(n_d, n_d - N_\beta)$	F statistic with n_d and $n_d - N_\beta$ degrees of freedom at the $100(1 - \kappa)\%$ confidence level
F_i	matrix that contains the first derivative of simulation output variables with respect to β , arranged so that derivatives with respect to the same parameter are in the same column
H	surface roughness, nm
i	current density, A/cm^2
k_j	rate constant for reaction j
M	degree of multivariate polynomial used for low-order model
M_i	number of measurements in experiment i
n	number of charge equivalents per mole
n_d	total number of data points
n_p	number of experiments
N	number of simulation data sets used in the identification of low-order model
N_β	number of model parameters β
p	parameter in response curve, dimensionless
r_H	size of deposited wafer, nm
$r_{H,k}$	k th spatial dimension of surface roughness
R	ideal gas constant, 8.314 J/mol K
$S(y_m, \beta_i)$	normalized sensitivity of model output y_m to the parameter β_i
$\bar{S}(i, \beta_i)$	sensitivity of current density with respect to parameter β_i averaged over the total number of points used for parameterizing time and spatial variations, A/cm^2
$\bar{S}(H, \beta_i)$	sensitivity of surface roughness with respect to parameter β_i averaged over the total number of points used for parameterizing time and spatial variations
t	time, s
$t_{1-\kappa/2}(n_d - N_\beta)$	t statistic with $n_d - N_\beta$ degrees of freedom at the $100(1 - \kappa)\%$ confidence level
t_m	m th deposition time, s
T	temperature, K
$V_{y,i}$	covariance matrix for the vector of output variables y for i th experiment
V_β	covariance matrix for the vector of parameters β
$V_{\beta,i}$	the $[i, i]$ element of V_β
$w_{i,j}$	weight factor on the noise level of the data in the parameter estimation objective
$y_{i,j}$	the j th numerical output (prediction) for the i th experiment: surface roughness (nm) current density (A/cm^2)
$y_{i,j}$	the j th experimental output (measured) for the i th experiment: surface roughness (nm) current density (A/cm^2)
\tilde{Y}_i	$[y_{i,1}, \dots, y_{i,M}]^T$, a vector of model outputs for the i th experiment
Greek	
α_j	transfer coefficient for reaction j , dimensionless
β	vector of model parameters to be estimated
β^*	the best estimate of β obtained after application of parameter estimation procedure
β_i	i th element of β
$\tilde{\beta}_i$	normalized i th element of β
$\Delta\beta_i$	relative size of a perturbation in parameter β_i , dimensionless ($0 < \Delta\beta_i < 1$)
η	surface overpotential, V
σ	electrolytic solution conductivity, $(\Omega \text{ cm})^{-1}$
θ	surface concentration of copper, mol/cm^2
v	time-varying stochastic input
Ψ	sum of squared errors in the output variables
Ψ^*	sum of squared errors in the output variables computed with the best parameter estimates β^*

References

1. R. Alkire, *J. Electroanal. Chem.*, **559**, 3 (2003).
2. R. C. Alkire and R. D. Braatz, *AICHE J.*, **50**, 2000 (2004).
3. P. C. Andricacos, C. Uzoh, J. Dukovic, J. Horkanes, and H. Deligianni, *IBM J. Res. Dev.*, **42**, 567 (1998).
4. P. M. Vereecken, R. A. Binstead, H. Deligianni, and P. C. Andricacos, *IBM J. Res. Dev.*, **49**, 3 (2005).
5. J. Reid, T. Entringer, and T. Rogelstad, *Plat. Surf. Finish.*, **90**, 445 (1990).

6. T. P. Moffat, D. Wheeler, and D. Josell, *J. Electrochem. Soc.*, **151**, C262 (2004).
7. R. Akolkar and U. Landau, *J. Electrochem. Soc.*, **151**, C702 (2004).
8. M. L. Walker, L. J. Richter, and T. P. Moffat, *J. Electrochem. Soc.*, **152**, C403 (2005).
9. T. P. Moffat, D. Wheeler, S. K. Kim, and D. Josell, *J. Electrochem. Soc.*, **153**, C127 (2006).
10. G. H. Gilmer, H. Huang, T. D. De la Rubia, J. D. Torre, and F. Baumann, *Thin Solid Films*, **365**, 189 (2000).
11. T. O. Drews, R. D. Braatz, and R. C. Alkire, *Int. J. Multiscale Comp. Eng.*, **2**, 313 (2004).
12. T. O. Drews, E. Webb, D. L. Ma, J. Alameda, R. D. Braatz, and R. C. Alkire, *AIChE J.*, **50**, 226 (2004).
13. X. Li, T. O. Drews, E. Rusli, F. Xue, Y. He, R. D. Braatz, and R. C. Alkire, *J. Electrochem. Soc.*, **154**, D230 (2007).
14. R. Gunawan, M. Y. L. Jung, E. G. Seebauer, and R. D. Braatz, *AIChE J.*, **49**, 2114 (2003).
15. D. Maroudas, *AIChE J.*, **46**, 878 (2003).
16. R. D. Braatz, R. C. Alkire, E. Seebauer, E. Rusli, R. Gunawan, T. O. Drews, X. Li, and Y. He, *J. Process Control*, **16**, 193 (2006).
17. Y. Qin, Ph.D. Thesis, University of Illinois at Urbana-Champaign, Urbana, IL (2006).
18. X. Li, Ph.D. Thesis, University of Illinois at Urbana-Champaign, Urbana, IL (2007).
19. F. Xue, Ph.D. Thesis, University of Illinois at Urbana-Champaign, Urbana, IL (2006).
20. W. Schmidt, Ph.D. Thesis, University of Illinois at Urbana-Champaign, Urbana, IL (1995).
21. O. R. Brown and H. R. Thirsk, *Electrochim. Acta*, **10**, 383 (1965).
22. M. Yokoi, S. Konishi, and T. Hayashi, *Denki Kagaku oyobi Kogyo Butsuri Kagaku*, **51**, 460 (1983).
23. C. Gabrielli, P. Mocoteguy, H. Perrot, and R. Wiart, *J. Electroanal. Chem.*, **572**, 367 (2004).
24. Z. Nagy, J. P. Blaudeau, N. C. Hung, L. A. Curtiss, and D. J. Zurawski, *J. Electrochem. Soc.*, **142**, L87 (1995).
25. J. J. Kelly and A. C. West, *J. Electrochem. Soc.*, **145**, 3472 (1998).
26. J. J. Kelly and A. C. West, *J. Electrochem. Soc.*, **145**, 3477 (1998).
27. Z. V. Feng, X. Li, and A. A. Gewirth, *J. Phys. Chem. B*, **107**, 9415 (2003).
28. K. R. Hebert, S. Adhikari, and J. E. Houser, *J. Electrochem. Soc.*, **152**, C324 (2005).
29. J. G. Long, P. C. Searson, and P. M. Vereecken, *J. Electrochem. Soc.*, **153**, C258 (2006).
30. S. Antonello, R. Benassi, G. Gavioli, F. Taddei, and F. Maran, *J. Am. Chem. Soc.*, **124**, 7529 (2002).
31. A. Frank and A. J. Bard, *J. Electrochem. Soc.*, **150**, C244 (2003).
32. J. P. Healy, D. Pletcher, and M. Goodenough, *J. Electroanal. Chem.*, **338**, 167 (1992).
33. E. E. Farndon, F. C. Walsh, and S. A. Campbell, *J. Appl. Electrochem.*, **25**, 574 (1995).
34. A. Survilla, S. Kanapeckaite, and R. Pauliukaite, *Chemija*, **1**, 21 (1998).
35. M. Kalke and D. V. Baxter, *Surf. Sci.*, **477**, 95 (2001).
36. A. C. Levi and M. Kotrla, *J. Phys.: Condens. Matter*, **9**, 299 (1994).
37. E. Rusli, Ph.D. Dissertation, University of Illinois at Urbana-Champaign, Urbana, IL (2006).
38. T. Maly and L. Petzold, *Appl. Numer. Math.*, **20**, 57 (1996).
39. H. S. Fogler, *Elements of Chemical Reaction Engineering*, 4th ed., pp. 904–922, Prentice Hall, Upper Saddle River, NJ (2006).
40. S. Raimondeau, P. Aghalayam, A. B. Mhadeshwar, and D. G. Vlachos, *Ind. Eng. Chem. Res.*, **42**, 1174 (2003).
41. T. O. Drews, R. D. Braatz, and R. C. Alkire, *J. Electrochem. Soc.*, **150**, C807 (2003).
42. A. Varma, M. Morbidelli, and H. Wu, *Parametric Sensitivity in Chemical Systems*, Cambridge University Press, Cambridge, U.K. (1999).
43. D. L. McLeish, *Monte Carlo Simulation and Finance*, John Wiley & Sons, Inc., Hoboken, NJ (2005).
44. S. Monni and S. Syri, Report VTT-TIED-RN-2209, p. 70, National Technical Information Service, U.S. Department of Commerce, Springfield, VA (2003).
45. J. V. Beck and K. J. Arnold, *Parameter Estimation in Engineering and Science*, Wiley, New York (1977).
46. R. H. Myers and D. C. Montgomery, *Response Surface Methodology Process and Product Optimization Using Designed Experiments*, John Wiley & Sons, Inc., New York (1995).
47. L. R. Bahl, R. Bakis, F. Jelinek, and R. L. Mercer, *IBM Tech. Discl. Bull.*, **1980**, 3464.
48. M. Y. L. Jung, R. Gunawan, R. D. Braatz, and E. G. Seebauer, *J. Appl. Phys.*, **95**, 1134 (2004).
49. K. Doblhofer, S. Wasle, D. M. Soares, K. G. Weil, and G. Ertl, *J. Electrochem. Soc.*, **150**, C651 (2003).
50. C. T. M. Kwok, K. Dev, R. D. Braatz, and E. G. Seebauer, *J. Appl. Phys.*, **98**, 013524 (2005).
51. R. D. Braatz, R. C. Alkire, E. G. Seebauer, T. O. Drews, E. Rusli, M. Karulkar, F. Xue, Y. Qin, M. Y. L. Jung, and R. Gunawan, *Comput. Chem. Eng.*, **30**, 1643 (2006).
52. R. Aris, *Mathematical Modelling Techniques*, Dover Publications, New York (1994).